A Semi-Langrangian Vortex Penalization Method for 3D Incompressible Flows

Chlo Mimeau[1,*], Iraj Mortazavi[1] and Georges-Henri Cottet[2]

[1] *Laboratoire M2N Modélisation, Mathématique et Numérique,*
Conservatoire National des Arts et Métiers, 292 Rue St Martin, 75003 Paris, France.
[2] *Laboratoire Jean Kuntzm ann, Univ. Grenoble Alpes and CNRS,*
700 Avenue Centrale, 38041 Grenoble, France.

Abstract. A remeshed Vortex method is proposed in this work to simulate three-dimensional incompressible flows. The convection equation is solved on particles, using a Vortex method, which are then remeshed on a Cartesian underlying grid. The other differential operators involved in the governing incompressible Navier-Stokes equations are discretized on the grid, through finite differences method or in spectral space. In the present work, the redistribution of the particles on the Cartesian mesh is performed using a directional splitting, allowing to save significant computational efforts especially in the case of 3D flows. A coupling of this semi-Lagrangian method with an immersed boundary method, namely the Brinkman penalization technique, is proposed in this paper in order to efficiently take into account the presence of solid and porous obstacles in the fluid flow and then to perform passive flow control using porous medium. This method, which combines the robustness of particle methods and the flexibility of penalization method, is validated and exploited in the context of different flow physics.

AMS subject classifications: 65M22, 35Q30, 76S05

Key words: Semi-Lagrangian method, remeshed Vortex method, penalization approach, bluff body flows, DNS.

1 Introduction

In recent years, improvements in computing enabled a large enhancement of numerical simulations related to Computational Fluid Dynamics (CFD). These simulations allow to predict the physical behavior of fluid flows. In the present study we particularly focus on

---

*Corresponding author. *Email addresses:* `chloe.mimeau@cnam.fr` (C. Mimeau), `iraj.mortazavi@cnam.fr` (I. Mortazavi), `georges-henri.cottet@univ-grenoble-alpes.fr` (G.-H. Cottet)

incompressible Newtonian fluid flows past obstacles, which have been and are still subject to many investigations due to their close relation to aerodynamic efficiency. In that sense, numerical simulations constitute a real economic issue when applied to engineering problems and are considered as interesting and reliable alternatives to wind-tunnel experimentations.

Among the numerous numerical approaches used in CFD, Lagrangian methods, also called particle methods, occupy an important place thanks to their intuitive and natural description of the flow. Indeed, in Lagrangian approaches, the physical quantities involved in the simulated problem are discretized onto a set of particles evolving spatially in the domain according to the problem dynamics. The particles are therefore characterized by their position in the computational domain and the value of the physical quantity they are carrying. Vortex methods [1] belong to this class of Lagrangian approaches and will constitute the key point of the present work. In vortex methods, the particles discretize the Navier-Stokes equations in their velocity (**u**) - vorticity (ω) formulation, closed with a Poisson equation allowing to recover the velocity of the fluid flow from the vorticity field. This formulation allows to directly point to the essence of vorticity dynamics in incompressible flows, which is characterized by advection and diffusion as well as stretching, which denotes the change of orientation. Another important feature of Lagrangian vortex methods lies in their low numerical diffusion [1, 2] and their stability.

However, vortex methods exhibit difficulties inherent to particle methods, mostly related to the treatment of the boundary conditions and the distortion of the particle distribution, which manifests itself by the clustering or spreading of the flow elements in high strain regions, thus implying the loss of convergence of the method. As demontrated first in [3] and later in [4], the convergence of Lagrangian vortex methods relies on the particles overlapping : if the vorticity carried by a particle is spacially distributed on a blob, that is to say on a disk of finite radius ε, then the convergence of vortex methods implies a strict relation between the particle spacing h and the blob radius ε, more precisely one must ensure $h = \mathcal{O}(\varepsilon)$. The remeshing technique [5, 6] may be considered as one of the most efficient and popular method to bypass the inherent problem of particle distribution distortion. It consists in periodically redistributing the particles onto an underlying Cartesian grid, while the momentum equation is solved in a Lagrangian framework, in order to ensure their overlapping and thus the convergence of the solution. These remeshed vortex methods involve a Lagrangian framework for the advection and stretching problems while handling also a fixed Cartesian grid. The presence of this grid facilitates the prescription of the no-slip boundary conditions as well as the modeling of the diffusive term and the resolution of the Poisson equation, using Eulerian schemes (e.g finite-differences, spectral methods, ...), and ensures the particle overlapping condition. In a computational point of view, the Cartesian grid also provides a simple and efficient framework in terms of implementation and parallelization.

In this work, we present a remeshed vortex method coupled with an immersed boundary technique in order to account for the presence of obstacles in the flow and to model the boundary conditions. The immersed boundary method chosen here is the Brinkman

penalization technique [7–9]. It relies on extending the fluid velocity inside the solid body and to solve the flow equations with a penalization term, depending on the intrinsic permeability, to enforce rigid motion inside the solid. Beyond the advantages specific to immersed boundary methods, the penalization approach allows to easily make the difference between the solid, fluid and also porous regions of the computational domain by defining the value of the penalization parameter without prescribing any explicit conditions at the interfaces. The simulation of 3D flows in a solid-porous-fluid domain is of great interest here in the context of passive flow control. As highlighted in [10], the presence of porous layers enables a damping of the flow-induced surface instabilities, therefore modifying the flow behavior in the vicinity of the solid-porous-fluid interface. Based on the works of [11, 12] (realized with a pure Eulerian approach), we propose in this work an application of our semi-Lagrangian vortex method to passive flow control, where the control device relies in a total or partial coating of a rear-view mirror-like geometry surface with a porous layer. Under optimal conditions related to the permeability of the added porous layer and its position, the modifications of the flow induced by the presence of such device may lead to a regularization of the wake and to a drag reduction.

The paper is organized as follows. In the first section we will give the governing equations as well as the algorithm and the numerical schemes proposed to discretize the problem. Section 3 is devoted to the numerical results. We will perform simulations for two different types of 3D flows: we will first study the Taylor-Green vortex case and then we will focus on flows past a solid hemisphere. For both flows, we perform a validation and a convergence study of the proposed method. The section related to the numerical results will end with an application to passive flow control past a hemispherical geometry using porous media. Finally, the computational cost associated to the implemented algorithm will be exposed in the last section of the paper.

2   Vortex penalization method

2.1   Governing equations

This study is based on the vorticity formulation of the incompressible Navier-Stokes equations with constant density, called the Vorticity Transport Equations. In a domain D, these equations read:

$$\frac{\partial \omega}{\partial t} + (\mathbf{u} \cdot \nabla) \omega - (\omega \cdot \nabla) \mathbf{u} = \frac{1}{Re} \Delta \omega \qquad \text{in } D, \qquad (2.1)$$

$$\Delta \mathbf{u} = -\nabla \times \omega \qquad \qquad \text{in } D, \qquad (2.2)$$

where ω, $\mathbf{u}$ and Re respectively denote the vorticity, the velocity and the Reynolds number. One can distinguish in equation (2.1) the advection term $(\mathbf{u} \cdot \nabla) \omega$, the stretching term $(\omega \cdot \nabla) \mathbf{u}$ (which vanishes in 2D) and the diffusion term $\Delta \omega / Re$. The Poisson equation

(2.2) is derived from the incompressibility condition $\nabla \cdot \mathbf{u} = 0$ and allows to recover the velocity field $\mathbf{u}$ from the vorticity field ω. This system of equations has to be complemented by appropriate boundary conditions, both at solid boundaries and at the boundaries of computational domain D. Let us notice that in 2D, the vorticity ω is a scalar field and that the stretching term therefore vanishes.

The modeling of incompressible flow around an obstacle is realized in this work using an immersed boundary method called the Brinkman penalization method [7,8]. With this technique the fluid is assumed to be a porous medium of infinite permeability while the solid obstacles immersed in the fluid are considered as media with zero permeability. A flow evolving in such media may be modeled by the Brinkman-Navier-Stokes equations, which stand for the whole computational domain and which contain an additional term with respect to the Navier-Stokes equations, acting as a forcing term. In this work, the penalization term is expressed in vorticity formulation. One therefore obtains the non-dimensional Brinkman-Vorticity Transport equations, originally proposed by [13]:

$$\frac{\partial \omega}{\partial t} + (\mathbf{u} \cdot \nabla)\omega - (\omega \cdot \nabla)\mathbf{u} = \nabla \times \left(\lambda \, \chi_b (\mathbf{u}_b - \mathbf{u}) \right) + \frac{1}{Re} \Delta \omega \qquad \text{in } D, \qquad (2.3)$$

$$\Delta \mathbf{u} = -\nabla \times \omega \qquad \qquad \text{in } D, \qquad (2.4)$$

where χ_b denotes the characteristic function that yields 0 in the fluid and 1 in the solid body, $\mathbf{u}_b$ indicates the rigid body velocity and $\lambda = \mu \Phi H / \rho k \mathbf{u}_\infty$ is the non-dimensional penalization parameter, with k the intrinsic permeability, μ the viscosity, Φ the porosity of the porous material, H the characteristic dimension of the obstacle, ρ the fluid density and $\mathbf{u}_\infty = (u_{x_\infty}, 0, 0)$ the main uniform fluid flow velocity field. In this study we set $H = \rho = u_{x_\infty} = 1$ and the porosity Φ is close to 1 as imposed by the Brinkman equation [14]. Therefore λ essentially depends, in the inverse proportion, on the intrinsic permeability k of the medium. We fix $\lambda = 0$ in the fluid region and $\lambda = 10^8$ in the solid region, which has been shown in previous studies [8, 15] to be a value leading the velocity to numerically converge to zero inside a solid region and at its boundaries.

The main advantage of the penalization method is that it needs neither the mesh to fit the boundaries nor to explicitly specify no-slip boundary conditions, which is of great interest in this context since the prescription of boundary conditions involving the velocity field is known to be a difficult issue in the context of vortex methods.

2.2 Splitting algorithm

To solve the penalized vorticity equations (2.3)-(2.4), the problem is discretized onto particles that carry the vorticity field ω transported at the velocity $\mathbf{u}$ and the resolution of the governing equations is based on a splitting algorithm [16–18], which consists at each

Table 1: Time and space discretization methods used for the resolution of the viscous splitting algorithm (equations (2.5) to (2.10)).

Equation	Time discretization method	Space discretization method
Poisson equation (2.5)	-	spectral method
Penalization (2.6)	implicit Euler scheme	4th order centered FD
Stretching (2.7)	RK3 scheme	4th order centered FD
Diffusion (2.8)	implicit Euler scheme	spectral method
Advection (2.9)	RK2 scheme	$\Lambda_{4,2}$ remeshed vortex method
Adaptive time step (2.10)	-	4th order centered FD (LCFL ≤ 1)

time step in successively solving the following equations:

$$\Delta \mathbf{u} = -\nabla \times \boldsymbol{\omega}, \tag{2.5}$$

$$\frac{\partial \boldsymbol{\omega}}{\partial t} = \nabla \times \left(\lambda \, \chi_b (\mathbf{u}_b - \mathbf{u}) \right), \tag{2.6}$$

$$\frac{\partial \boldsymbol{\omega}}{\partial t} = (\boldsymbol{\omega} \cdot \nabla) \mathbf{u}, \tag{2.7}$$

$$\frac{\partial \boldsymbol{\omega}}{\partial t} = \frac{1}{Re} \Delta \boldsymbol{\omega}, \tag{2.8}$$

$$\frac{\partial \boldsymbol{\omega}}{\partial t} + (\mathbf{u} \cdot \nabla) \boldsymbol{\omega} = 0, \tag{2.9}$$

$$\Delta t_{\text{adapt}} = \frac{\text{LCFL}}{\|\nabla \mathbf{u}\|_{\infty}}. \tag{2.10}$$

The discretization of each equation of the splitting algorithm is realized in this study by using a semi-Lagrangian vortex method, called the remeshed vortex method. Table 1 gives the time and space discretization schemes used in this work to solve them. Figure 1 also shows a schematic representation of the overall algorithm.

The advection of vorticity field (equation (2.9)) is performed in a Lagrangian way using
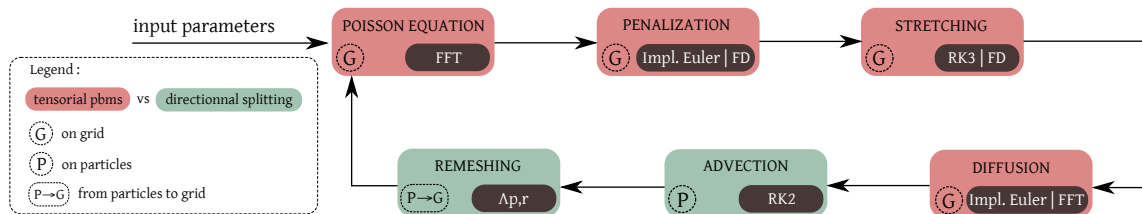

Figure 1: Sketch of the splitting algorithm.

a vortex method :

$$
\begin{cases}
\dfrac{dx_p}{dt} = u_i^n(x_p), & \forall i \in \{1,2,3\}, \\
x_p^{n+1} = x^{n+1}, \\
\omega_i^{n+1} = \displaystyle\sum_p \omega_p^n \Lambda_{4,2}\left(\dfrac{x_p^{n+1} - x_i}{h}\right).
\end{cases}
\tag{2.11}
$$

Once the particle positions x_p have been updated according to the flow velocity (cf. first equation of system (2.11)), the vorticity carried by each particle is redistributed on the neighbouring points of the underlying cartesian grid using a remeshing kernel of type $\Lambda_{p,r}$ [19] (cf. last equation of system (2.11)). The $\Lambda_{p,r}$ remeshing kernels are piecewise polynomial functions of regularity $\mathcal{C}^r$, satisfying the conservation of the first p moments. In this work, the particle advection and the remeshing procedure are performed using a directional splitting approach [20]. It consists in successively solving 1D convection/remeshing problems, direction by direction, as written in equations (2.11). As a consequence, if the chosen kernel contains S points in its 1D-support, the number of operations with the directional splitting method goes from $\mathcal{O}(S^2)$ to $\mathcal{O}(2S)$ in 2D and from $\mathcal{O}(S^3)$ to $\mathcal{O}(3S)$ in 3D. This directional splitting therefore allows a significant reduction of the computational efforts compared to the more traditional remeshing procedure based on tensor product formulas.

The systematic remeshing of particles onto an Eulerian grid at each time step after the advection stage, enables to ensure the overlapping of particles required for the convergence of the method. Moreover the presence of the grid allows to discretize the other equations using efficient and/or fast grid methods (finite differences and spectral method based on FFT evaluations). In the present algorithm, equations (2.5) to (2.8) are solved on the grid.

The Poisson equation (2.5) is first resolved in the Fourier space according to the following expression :

$$
\widehat{\mathbf{u}}(\xi) = \frac{1}{|\xi|^2}(\widehat{\boldsymbol{\nabla} \times \boldsymbol{\omega}}).
\tag{2.12}
$$

The penalization of the vorticity field (equation (2.6)) naturally satisfies the desired boundary conditions by prescribing the correct values of λ in the different regions of the domain (solid-porous-fluid), as explained in the previous section. In this paper we only consider static immersed obstacles, therefore the velocity of the body is $\mathbf{u}_b = 0$. The conservative formulation of the discrete penalized vorticity writes:

$$
\boldsymbol{\omega}^{n+1} = \boldsymbol{\omega}^n + \boldsymbol{\nabla} \times \left(\frac{-\lambda \chi_b \Delta t\, \mathbf{u}^n}{1 + \lambda \chi_b \Delta t}\right),
\tag{2.13}
$$

where $\mathbf{u}^n$ denotes the velocity recovered from (2.12) after performing an inverse Fourier transform. The treatment of this penalization equation is realized using a 4th order centered finite-differences scheme for the discretization of the curl operator. We notice that

the velocity field is not directly penalized in this algorithm. The velocity penalization is implicitly realized through the resolution of the Poisson problem (2.5). With the penalization approach, the treatment of boundary conditions is therefore efficient in terms of modeling (one has a unique equation available in the whole computational domain), of computational cost (we refer the lecturer to the last section of this paper dedicated to the computational resources of the overall method) and also in terms of implementation and parallelization efforts.

The stretching problem (2.7) is considered here in its conservative formulation :

$$\frac{\partial \boldsymbol{\omega}}{\partial t} = \mathrm{div}(\boldsymbol{\omega}\!:\!\mathbf{u}), \tag{2.14}$$

where $\mathrm{div}(\boldsymbol{\omega}\!:\!\mathbf{u}) := (\boldsymbol{\omega}\cdot\nabla)\mathbf{u} + \mathbf{u}\,\mathrm{div}(\boldsymbol{\omega})$, and a solenoidal reprojection based on the Helmholtz decomposition of the vorticity field is done in the Fourier space every timestep in order to ensure a divergence-free vorticity field ($\mathrm{div}(\boldsymbol{\omega}) = 0$). The time integration scheme chosen here to discretize this equation is the 3rd order Runge-Kutta TVD (Total Variation Diminishing, i.e. non extra oscillations) scheme. With this time discretization, the velocity field involved in the divergence operator is not modified. The divergence operator is discretized through a 4th order centered finite-diffrences scheme on the grid.

Concerning the diffusion equation (2.8), it is discretized in time using an implicit 1st order Euler scheme:

$$\frac{\boldsymbol{\omega}^{n+1} - \boldsymbol{\omega}^n}{\Delta t} = \frac{1}{Re}\Delta\boldsymbol{\omega}^{n+1}, \tag{2.15}$$

$$\Longleftrightarrow \quad \Delta\boldsymbol{\omega}^{n+1} - \frac{Re}{\Delta t}\boldsymbol{\omega}^{n+1} = -\frac{Re}{\Delta t}\boldsymbol{\omega}^n. \tag{2.16}$$

This equation is solved in the Fourier space, where the solution is given by

$$\hat{\boldsymbol{\omega}}^{n+1} = \frac{\frac{Re}{\Delta t}}{|\xi|^2 + \frac{Re}{\Delta t}}\,\hat{\boldsymbol{\omega}}^n. \tag{2.17}$$

An adaptive time-step $\Delta t_{\mathrm{adapt}}$ is computed at the end of the fractionnal step algorithm (2.10). It is based on the non-linear stability of the advection/remeshing scheme in vortex methods :

$$\Delta t_{\mathrm{adv}} \leq \frac{\mathrm{LCFL}}{\|\nabla\mathbf{u}\|_\infty}, \tag{2.18}$$

where the LCFL denotes the Lagragian CLF [21]. This number must satisfy $\mathrm{LCFL}\leq 1$ [19]. From a physical point of view, this stability condition imposes that particles trajectories do not cross. As the time step defined by this stability condition is not constrained by the grid size or the distance between the particles but only by the flow strain, it often provides larger time steps compared to Eulerian schemes, based on CFL conditions.

Concerning far-field boundary conditions, the present study uses a bounded plane-parallel computational domain to solve the Brinkman vorticity transport equations (2.3)-(2.4). Artificial boundary conditions therefore need to be prescribed at the box walls. In the present work, we prescribe periodic boundary conditions on the domain walls. This choice allows us to use a Fast Fourier Transform (FFT) method to efficiently solve the Poisson equation $\Delta u = -\nabla \times \omega$. As a consequence, handling periodic boundary conditions implies special treatments on the flow fields in order to recover the desired uniform flow at the inlet: on one hand the eddies coming periodically from the outlet are discarded with a smooth absorption and on the other hand the velocity flux is corrected at the inlet so as to recover the desired incoming uniform flow. More details about this method may be found in [22].

3   Numerical results

In order to verify the convergence, accuracy and efficiency of the method, we present in this section a numerical validation study based on Direct Numerical Simulations (DNS). These simulations concern two different types of flows. First we analyze the performances of the method in the case of the Taylor-Green vortex benchmark, an unbounded periodic flow commonly used to study the capability of a numerical method to handle transition to turbulence. The second part of this section is related to bluff body flows at transitional and subcritical regimes in order to test the ability of the present penalization-vortex method to simulate flows around immersed obstacles. We will more precisely focus on flow around a 3D hemisphere ; some validation results will be given and an application to passive flow control using porous media will also be presented.

3.1   Taylor-Green vortex

The Taylor-Green vortex is an analytical periodic solution of the incompressible Navier-Stokes equations. It describes the non-linear interaction of multiscales eddies under the influence of vortex stretching and their final decay. It is a classical benchmark used as an initial condition for numerical methods to study flow problems related to transition to turbulence. This bencharmark has already been tested with success in the context of a remeshed vortex method by van Rees *et al.* [17]. Since this method was different from the present one in the sense of the remeshing procedure (tensorial versus directional approach in our case), we test hereafter the validity of the method proposed in this work.

We consider the flow that evolves in a periodic cubic box of side length $L = 2\pi$ and develops from the following initial condition, which satisfies the divergence-free constraint:

$$
\begin{aligned}
u_x(\mathbf{x}, t=0) &= \sin(x)\cos(y)\cos(z), \\
u_y(\mathbf{x}, t=0) &= -\cos(x)\sin(y)\cos(z), \\
u_z(\mathbf{x}, t=0) &= 0.
\end{aligned}
\tag{3.1}
$$

The Reynolds number of the flow is defined by $Re = 1/\nu$. In the present study it is set to $Re = 1600$. At such regime, the minimum number of grid cells required per direction in DNS is approximatly given by

$$n_x \approx \frac{l_0}{\eta} = Re^{3/4} \sim 253, \tag{3.2}$$

where $l_0 = 1$ denotes the integral length scale, that is to say the scale of the largest eddies, and where $\eta = \left(\nu^3 l_0 / u_0^3 \right)^{\frac{1}{4}}$ corresponds to the Kolmogorov length scale, that is to say the scale of the smallest eddies, with u_0 the caracteristic velocity set to 1. Therefore, according to this estimation, we expect reliable results from a 253^3 total grid resolution. Concerning the numerical time step, the simulations performed in this work are based on an adaptative time step defined by equation (2.10) with a LCFL value set to 0.125.

Let us first describe the physics of the flow at $Re=1600$. The different stages explained hereafter are illustrated by Figures 2a and 3 obtained from simulations performed with the present method taking $n_x = n_y = n_z = 256$ and LCFL $= 0.125$ for spacial and time discretization respectively, and respectively depicting the kinetic energy dissipation rate $\varepsilon = -dE/dt$ and the magnitude of the 3D vorticity field. After a short laminar stage (Figure 3a), the vortices roll-up and start to interact with each others under the influence of the vortex stretching, leading to an important change in their topology with lengthening and thinning of the vortical structures (Figure 3b). It corresponds to the beginning of the energy cascade. Then the viscous stage arises and regions of high energy dissipation are formed until the maximum of dissipation is reached at $T \approx 9$ (Figure 3c) and kinetic energy is dissipated into heat under the action of molecular viscosity. After the dissipation peak, the coherent eddies are deformed and destroyed leading to the developed turbulent flow, which starts to mix and decay from $T \approx 12$ (Figure 3d). The similar analysis given in [23] may be cited as a first qualitative validation of the present results.

Let us now focus on the adativity of the time step Δt_{adapt} according to the flow physics. Figure 2b gives the evolution of the adaptative time step, which depends on the infinite norm of the velocity gradient, $\|\nabla \mathbf{u}\|_\infty$ (cf. equation (2.10)). Let us consider the value of Δt_{adapt} obtained at a given time t with a given and fixed LCFL number (LCFL $= 0.125$ here), then one can define the equivalent CFL number as $\text{CFL}_{eq} = \Delta t_{\text{adapt}} \|\mathbf{u}\|_\infty / \Delta x$, where $\|\mathbf{u}\|_\infty$ denotes the infinite norm of the velocity field. We can clearly see on Figure 2b that rather large time steps are taken at the beginning of the simulation (where $\|\mathbf{u}\|_\infty \sim 1$) with an equivalent CFL close to 0.5, whereas at $T=8$, when the peak of energy dissipation is almost reached and the multiscale structures interact with each others, the adapative time step decreases to its minimum value which is equivalent to $\text{CFL}_{eq} = 0.2$. At the end of the simulation, the equivalent CFL is approximately equal to 0.37. The formulation (2.10) of the adaptive time-step therefore ensures at any time the stability of the method and the precision of the solution while enabling fast computations when the flow strain is relatively low.
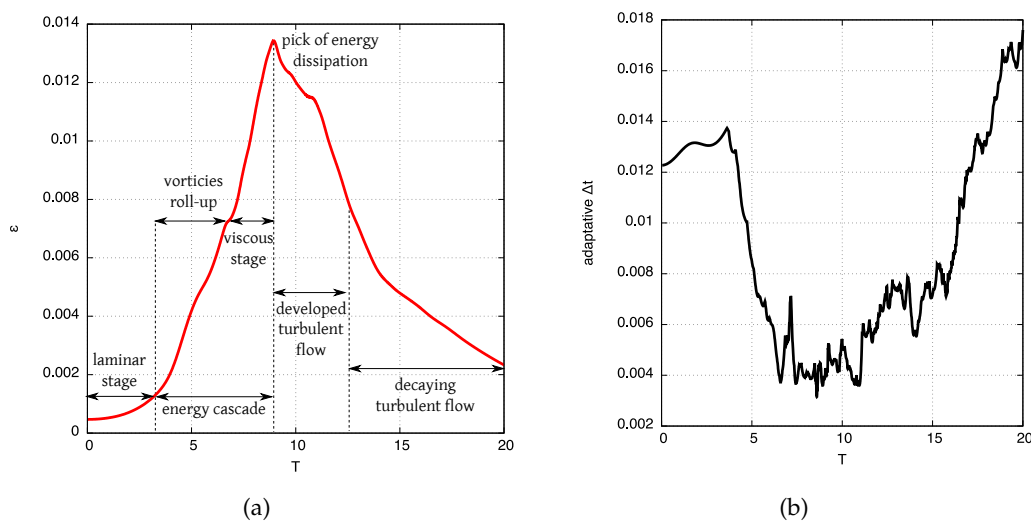
(a)   (b)

Figure 2: Taylor-Green vortex at $Re = 1600$. (a) Time evolution of the kinetic energy dissipation rate ε. (b) Evolution of adaptative time step Δt.

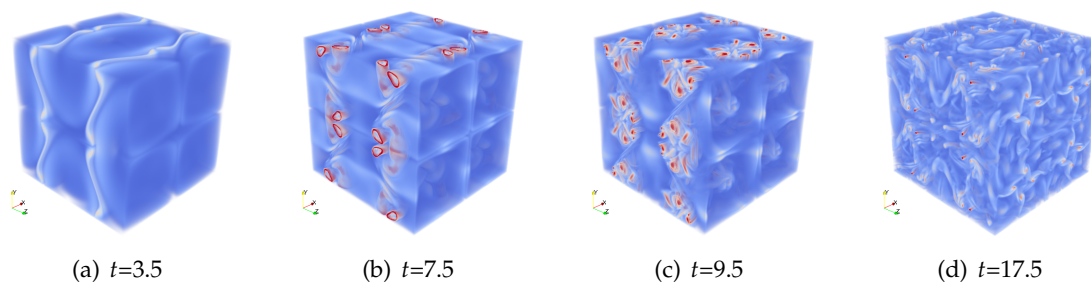(a) t=3.5   (b) t=7.5   (c) t=9.5   (d) t=17.5

Figure 3: Instantaneous magnitude of vorticity field $|\omega|$ at different stages of the Taylor-Green vortex simulation at $Re = 1600$.

3.1.1 Grid convergence study

In the present grid convergence study the simulations are performed on the following uniform Cartesian grids:

$$n_x \times n_y \times n_z = 64^3, \ 128^3, \ 256^3, \ 512^3.$$

The results are analyzed in terms of enstrophy evolution, where the enstrophy is the integral quantity defined as:

$$Z = \frac{1}{L^3} \int_D \boldsymbol{\omega}^2 \, d\mathbf{x} = \nu^{-1} \varepsilon. \tag{3.3}$$

They are compared in Figure 4 to the convergence study performed by Jammy *et al.* using an explicit finite difference solver [24]. We can notice that both methods converge

with a 256^3 resolution, which corresponds to the minimum number of cells required in the domain to correctly solve the smallest scales, as explained previously. One can also emphasize an interesting feature of the vortex methods which relies on the fact that even with unconverged grids (e.g. 64^3), the correct maximum value of enstrophy at $T \approx 9$ is captured by the present method (Figure 4a), which is not the case with a finite difference based method (Figure 4b).
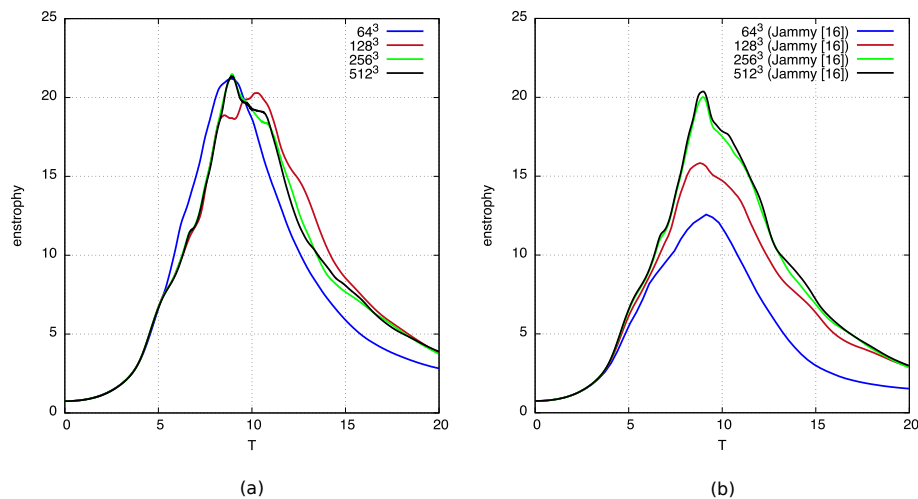

Figure 4: Grid convergence study in terms of enstrophy evolution. (a) Present method. (b) Results obtained by [24] with the OpenSBLI solver, based on a finite difference algorithm.

3.1.2 Validation

Based on the results of the previous section, we consider the converged grid $n_x \times n_y \times n_z = 512^3$ for the simulations performed in this validation study. First, we compare our results with [24] in terms of kinetic energy decay and integral enstrophy. As can be seen on Figure 5, the two solutions are in good agreement, especially until $T \approx 9$, when the peak of energy dissipation is reached. A discrepancy between the two results is then observed during the flow mixing stage, showing a slightly more antidiffusive behavior provided by the present vortex method compared to the finite difference method of [24] reported here or the spectral methods evoqued in [17, 25].

Our results are now qualitatively analyzed in terms of vortical structures in the flow. Figure 6a shows the norm of vorticity field $|\omega|$ in the $x=0$ plane at $T=8$, obtained with the present method using a 512^3 resolution. The vorticity isocontours of the eddy depicted on the close-up view are given below, in Figure 6b, and are compared to the one found in [17] using also a semi-Lagrangian vortex method at the same resolution of 512^3 (see Figures 6c and 6d). The same comparisons are made in Figure 7 for vortical structures obtained at $T=9$, when the maximum of energy dissipation occurs. These instantaneous snapshots and isocontours correspond to times when the most complex vortical eddies
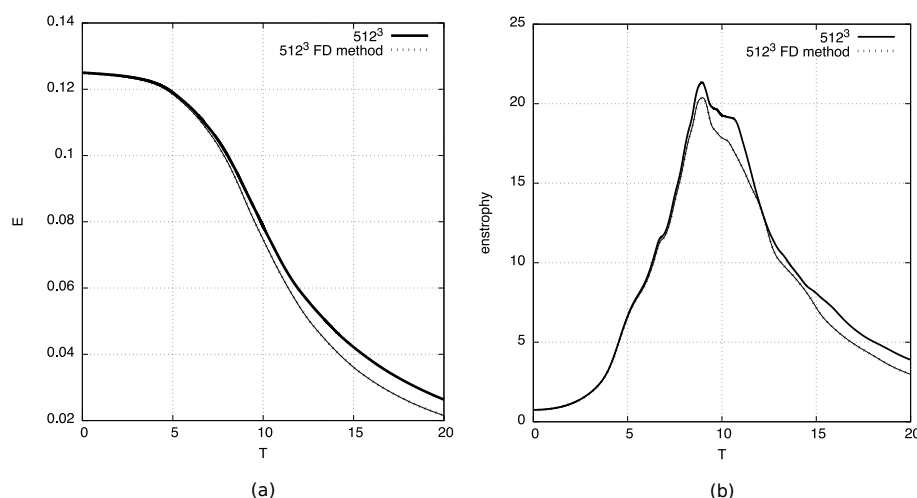
Figure 5: Comparison of the present method results (solid lines) with the one based on finite difference method in [24] (dashed lines). (a) Time evolution of the decay of kinetic energy. (b) Time evolution of integral enstrophy.

are formed in the flow.

As can be noticed, our results and the one of [17] coincide rather well, both at $T = 8$ and $T = 9$. The global size of the eddy and the thin elongated parts on the right are almost similar for both methods. A noticeable discrepancy is however noticed concerning the shape of the "eye" of the vortical structure, which is related to the slight overprediction of the energy dissipation of the present method (cf. Figure 5). However, no spurious oscillations are observed in the present vorticity isocontours.

3.2 Flow past a hemisphere

In this section, the present remeshed vortex method is validated in the context of three dimensional flows past solid bluff bodies. More precisely we consider the case of a 3D flow past a hemisphere whose bluff surface is facing upstream and flat surface is oriented downstream [26]. Due to the presence of a flat back wall with sharp edges, the flow past a hemisphere is a steeper problem compared to the flow past a sphere and is therefore challenging from a numerical point of view. Our purpose in this section is to measure to which extent the penalization method can handle this type of singularity in three dimensions, at transitional Reynolds numbers.

3.2.1 Numerical setup

In the sequel, the simulations are performed in a 3D computational box $D = [-2, 8.24] \times [-2.56, 2.56] \times [-2.56, 2.56]$, meshed by an uniform Cartesian grid. The hemisphere is centered at the origin of the computational domain. The non-dimensional diameter of the obstacle is set to $d = 1$ and the free stream velocity is equal to $\mathbf{u}_\infty = (u_{x\infty}, u_{y\infty}, u_{z\infty}) = (1,0,0)$.
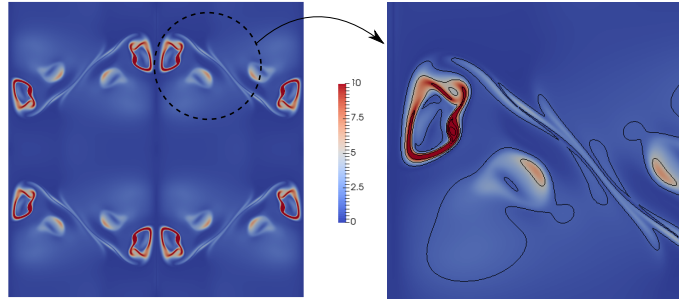
(a) Global view (left) and close up view (right) of $|\boldsymbol{\omega}|$ at $T=8$ in the $x=0$ plane using the present method with a 512^3 resolution.

(b) Present method   (c) Results obtained by [17]   (d) Superimposition of present result and [17]
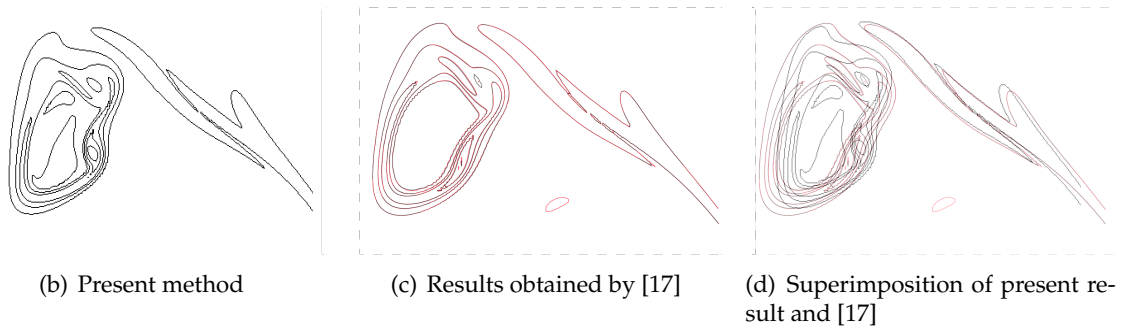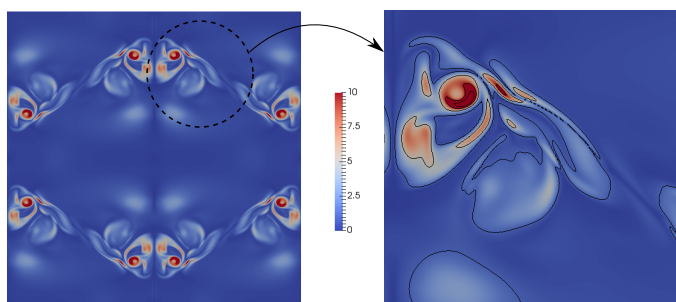
Figure 6: Instantaneous magnitude of vorticity field $|\boldsymbol{\omega}|$ at $T=8$ in the $x=0$ plane with a 512^3 resolution. In subfigures (b), (c) and (d) the isocontours of $|\boldsymbol{\omega}|$ are plotted for values of 1, 5, 10, 20, 30.

As mentionned previously, the bluff surface of the hemisphere faces the upstream flow and the flat one is oriented downstream. As in [27], a perturbation is addressed to the uniform upstream flow between the non-dimensional time $T=3$ and $T=4$, in order to trigger the instability. This perturbation is applied on the y component of the velocity and is expressed as $u_{y\infty}=\sin(\pi(T-3))$. The time step is defined according to equation (2.10), with LCFL $=0.125$. It is approximately equal to $\Delta t_{\text{adapt}} \approx 0.011$ all along the simulation. The penalization parameter is set to $\lambda = 10^8$ in the solid hemisphere.

The results of this section will be interpreted in terms of different physical quatitites : the Strouhal number $S_t=fd/u_{\infty}$, the enstrophy $Z=\int_D |\boldsymbol{\omega}|^2\,d\mathbf{x}$ and the aerodynamic forces, namely the drag coefficient C_D, the vertical lift coefficient C_L and the side lift coefficient C_S :

$$C_D = \frac{2F_x}{\rho u_{\infty}^2 \mathcal{A}}, \quad C_L = \frac{2F_y}{\rho u_{\infty}^2 \mathcal{A}}, \quad C_S = \frac{2F_z}{\rho u_{\infty}^2 \mathcal{A}}, \tag{3.4}$$

where $\mathcal{A}$ corresponds to the surface area of the circular back face of the hemisphere.

(a) Global view (left) and close up view (right) of $|\boldsymbol{\omega}|$ at $T=9$ in the $x=0$ plane using the present method with a 512^3 resolution.
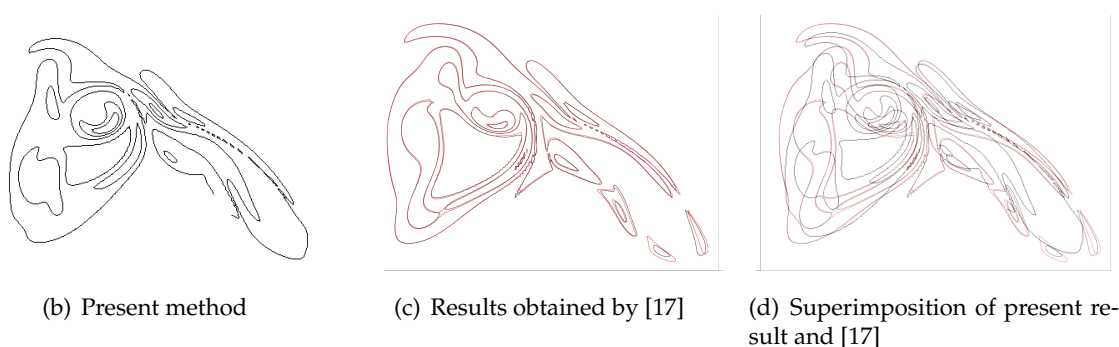

(b) Present method   (c) Results obtained by [17]   (d) Superimposition of present result and [17]

Figure 7: Instantaneous magnitude of vorticity field $|\boldsymbol{\omega}|$ at $T=9$ in the $x=0$ plane with a 512^3 resolution. In subfigures (b), (c) and (d) the isocontours of $|\boldsymbol{\omega}|$ are plotted for values of 1, 5, 10, 20, 30.

Concerning the aerodynamic forces F_x, F_y and F_z exerced on the hemisphere and involved in the above expressions, they are computed in the present study by integrating in the solid body $\mathcal{B}$ the difference between the flow velocity $\mathbf{u}$ and the numerical penalized velocity $\mathbf{u}_\lambda = \dfrac{\mathbf{u}}{1+\lambda\Delta_t}$ [28] :

$$F = \frac{d}{dt}\int_{\mathcal{B}} (\mathbf{u}-\mathbf{u}_\lambda)\, d\mathbf{x}. \tag{3.5}$$

The evaluation of this force is performed right after the resolution of the penalization equation (2.6) in the splitting algorithm described in Section 2.2.

3.2.2 Grid convergence study

A grid convergence study is performed for flow past a 3D hemisphere at $Re=300$. It involves four mesh sizes $h=0.08$, $h=0.04$, $h=0.02$ and $h=0.01$, which correspond to global resolutions ranging from $n_x \times n_y \times n_z = 128 \times 64 \times 64$ to $1024 \times 512 \times 512$ in the domain D. Convergence orders are determined by computing the L^1, L^2 and L_∞ norms of the error of

Table 2: Convergence study for flow past a hemisphere at $Re = 300$. $\bar{C_D}$ and $\bar{Z}$ respectively denote the mean values of drag coefficient and enstrophy.

	$Re = 300$	
Grid	$\bar{c_D}$	$\bar{Z}$
$h = 0.08$ $(n_x \times n_y \times n_z = 128 \times 64 \times 64)$	0.787	73.4
$h = 0.04$ $(n_x \times n_y \times n_z = 256 \times 128 \times 128)$	0.725	73.0
$h = 0.02$ $(n_x \times n_y \times n_z = 512 \times 256 \times 256)$	0.721	73.3
$h = 0.01$ $(n_x \times n_y \times n_z = 1024 \times 512 \times 512)$	0.725	74.0

two different flow quantities, namely the enstrophy Z and the drag coefficient C_D, with respect to the best resolved case ($h = 0.01$):

$$e(t) = \| \, q_{\text{best resolved}}(t) - q(t) \, \|, \tag{3.6}$$

where the quantity q either denotes the drag coefficient C_D or the enstrophy Z.

The order of convergence for the drag coefficient is found to be 1.80 for L^1, 2.23 for L^2, 1.48 for L_∞ and 0.95 for L^1, 1.49 for L^2, 1.23 for L_∞ concerning the enstrophy. They are complemented by Table 2, giving the converged mean values of the two flow quantities at $Re = 300$. On the basis of these results one may consider that the grid convergence is roughly obtained by setting $h = 0.04$.

3.2.3 Validation

To our knowledge there are only few experimental and numerical results dedicated to the problem of flow past a 3D hemisphere. This section is based on the study carried out by Kim & Choi [26], who investigated in detail the behavior of flows past a hemisphere at different low and transitional Reynolds numbers, ranging from 100 to 300.

Flow past a hemisphere at $Re = 200$ and 300

In this validation study we will focus on Reynolds numbers 200 and 300, corresponding to different unsteady flow behaviors. These Reynolds numbers are also studied in detail in [26]. Based on the grid convergence study reported in Table 2, the simulations presented in this validation section are performed with a mesh resolution set to $n_x \times n_y \times n_z = 512 \times 256 \times 256$, in order to better capture the boundary layer.

The flow at $Re = 200$ is first considered. Table 3 gives the mean values of the force coefficients at $Re = 200$ and one can notice a very good agreement between the present results and those of [26]. Concerning the Strouhal number, one can see in our case and in the reference results that the Strouhal based on the lift is half the one based on the drag. Finally, we focus on the side lift coefficient C_S. At $Re = 200$ the time average of this coefficient is not zero, which corroborates the fact that the flow does not maintain the planar-symmetry. This statement is confirmed by Figure 8 depicting the vorticity norm
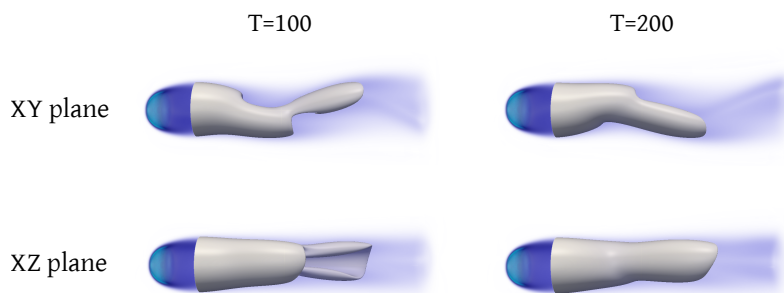
Figure 8: Instantaneous 3D vortical structures with isocontour $|\omega|=0.8$ for flow past a hemisphere at $Re=200$.

$|\omega|$ at two different times, where one can see that the wake is not symmetric in the plane XZ at this Reynolds number.

At $Re=300$, the flow has a more complex behavior. The vorticity norm reported in Figure 9 highlights the absence of any planar-symmetry. The same behavior is observed in [26]. On the other hand, Table 3 reveals that, at this regime, there co-exist two distinct values of the Strouhal number based on the power spectrum of the drag. The lower frequency ($St_{\text{drag1}}=0.04$) is due to the large-scale instability of the wake, while the higher frequency ($St_{\text{drag2}}=0.270$) is attributed to the small-scale instabilities caused by the separation of the shear layer. The St_{drag2} value is still approximately equal to twice the dominant frequency of the lift ($St_{\text{lift}}=0.135$). One can also remark in Table 3 that the time average lift coefficient $\bar{C}_L$ is approximately zero, like for $Re=200$. Indee d, the vortices shed alternatively with the same strength in the flow direction (cf. Figure 8 and 9 in XY plane), leading to $\bar{C}_L \approx 0$.

Flow past a hemisphere at $Re=1000$

In our last investigation, we aim to extend our study to non-laminar flows past hemisphere. To our knowledge, no study has been carried out experimentally or numerically at such regimes, and more generally at a Reynolds number larger than $Re=300$. The simulation presented here is performed at $Re=1000$, which is expected to belong to a

Table 3: Comparison of mean drag and lift coefficients as well as Strouhal numbers for flow past a hemisphere at $Re=200$ and 300.

$Re=200$	$\bar{c}_D$	$\bar{c}_L$	$\bar{c}_S$	St_{lift}	St_{drag}	
Kim & Choi [26]	0.790	0.0 ± 0.024	0.049	0.128	0.256	
Present	0.805	0.003 ± 0.025	0.043	0.129	0.257	

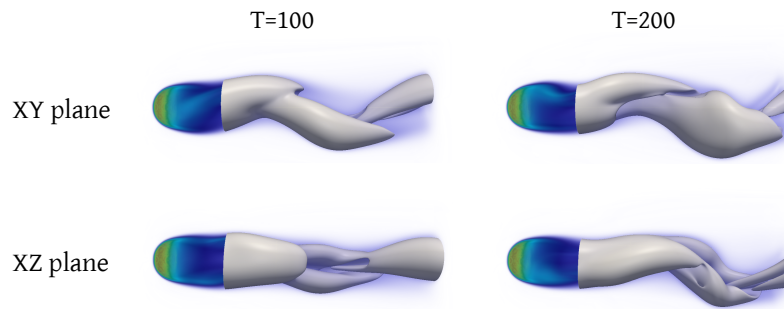| $Re=300$	$\bar{c}_D$	$\bar{c}_L$	$\bar{c}_S$	St_{lift}	St_{drag1}	St_{drag2}
Kim & Choi [26]	0.715	0.0 ± 0.062	0.0	0.135	0.04	0.270
Present	0.729	-0.002 ± 0.063	-0.0016	0.134	0.04	0.270

Figure 9: Instantaneous 3D vortical structures with isocontour $|\omega|$=0.8 for flow past a hemisphere at Re=300.
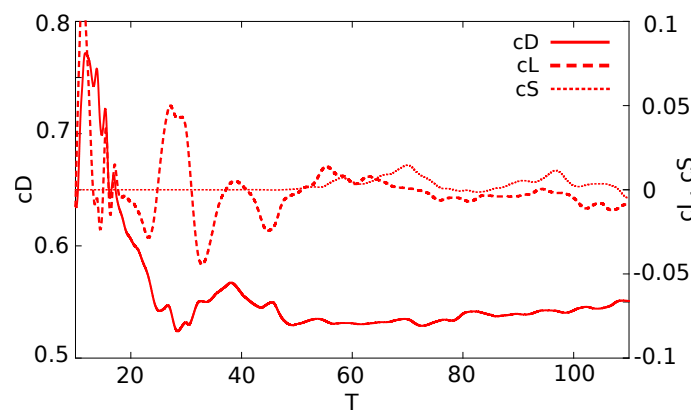

Figure 10: Time evolution of the aerodynamic coefficients for flow past a hemisphere at Re=1000.

range of transitional Reynolds numbers responsible for the apparition of a secondary instability in the shear wake, propagating in the wake. On the basis of the grid refinement study reported in Table 2, we have set for this case the mesh resolution to $n_x \times n_y \times n_z = 1024 \times 512 \times 512$. The results indicate that the flow past a hemisphere at Re=1000 is unsteady, non-periodic and asymmetric. The time history of the force coefficients is reported in Figure 10. It indeed shows that from $T \simeq 55$ the wake becomes chaotic and is characterized by important and non-periodic variations of the side lift coefficient C_S.

Figure 11 depicts the isocontours of the streamwise vorticity past a hemisphere in the XZ plane at different times. One can verify in particular that, as suggested by the evolution of the side lift coefficient C_S (see Figure 10), the wake looses its symmetry between T=40 and T=60. The delayed asymmetric behavior can be explained by the flat back wall of the hemisphere and seems triggered by the insight of secondary instabilities in the shedding shear areas.
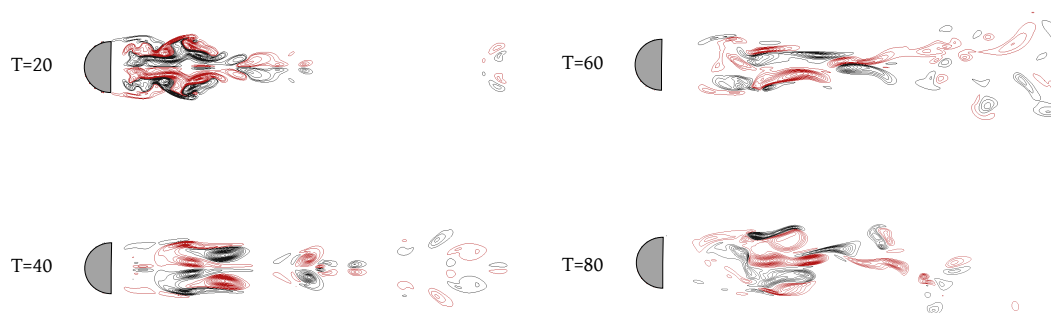
Figure 11: Isocontours of ω_x in the XZ plane for flow past a hemisphere at $Re\!=\!1000$.

3.3 Passive flow control using porous media

The present version of vortex penalization method can be used to efficiently perform flow simulations in a solid-fluid-porous domain. Indeed, the Brinkman-Navier-Stokes equations (2.3)-(2.4) appears to be very convenient to model the flow in complex media thanks to the dimensionless penalization factor λ, whose value allows to distinguish between the different materials. Setting the λ parameter to an intermediate value, reasonably chosen between the two extreme values $\lambda = 0$ (fluid domain) and $\lambda\!=\!10^8$ (solid domain), allows to model a porous medium in which the flow has a non-zero Darcy velocity.

Here, the simulation of flows in solid-fluid-porous media is applied to a 3D passive flow control study consisting in covering the surface of a side-view mirror geometry (modeled by a hemisphere) with a porous coating in order to change the flow properties at the boundary and to achieve drag reduction. Figure 12 shows the different geometrical configurations considered in this flow control study. The simulations are performed at $Re\!=\!1000$ using the same parameters as the one given in Section 3.2.3. As Figure 13 shows, the porous ring inlay configuration provides better results in terms of flow control (important decrease of vorticity values in the wake (Figure 13a) and a drag force reduction of 16% (Figure 13b) compared to the homogeneous porous layer. This outcome may be explained by the position of the porous zone on the hemisphere surface: indeed, in the ring inlay configuration, the permeable region is only located in the vicinity of the separation points, preventing from the resistance phenomenon experienced by the fluid in the front part of the hemisphere in the porous layer case.

4 Computational resources

In this last section, we focus on the computational cost of the proposed method. The direct numerical simulations presented in this paper were performed on bi-Xeon Sandy-Bridge cores. Table 4 gives the numerical setup, the resources and the CPU time-to-solution for the 3D flows around a hemisphere analyzed in this work. Let us remind
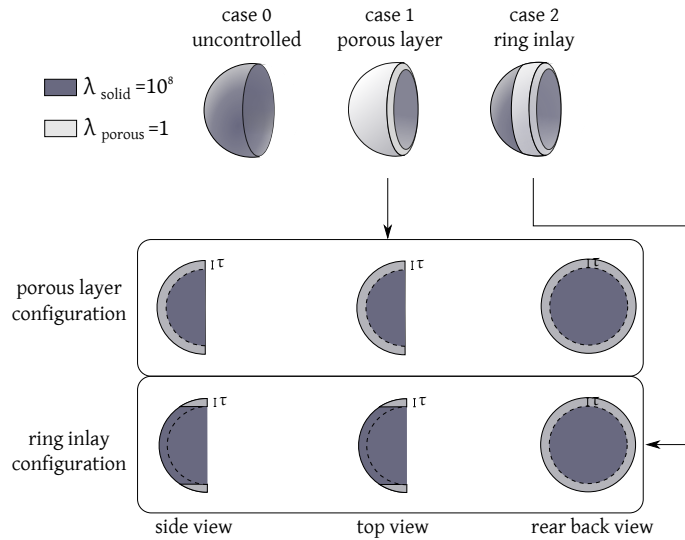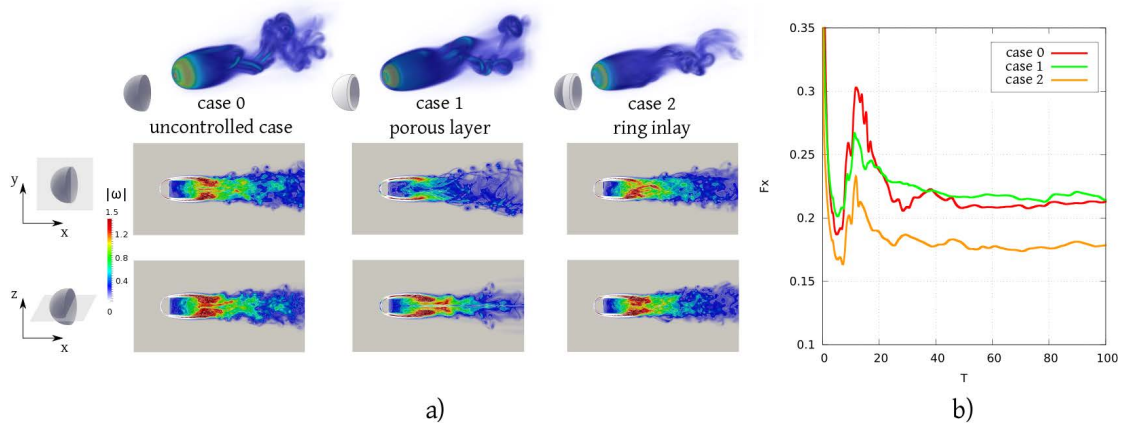
Figure 12: Flow control geometrical configurations. Case 0 depicts the uncontrolled case and cases 1 and 2 correspond to different porous layer configurations.

(a) Global view (left) and close up view (right) of $|\boldsymbol{\omega}|$ at $T=9$ in the $x=0$ plane using the present method with a 512^3 resolution.

(b) Present method

Figure 13: Passive control using porous media around a 3D hemisphere (simplified side-view mirror geometry) at $Re=1000$. The flow past an uncontrolled hemisphere (case 0) is compared to the flow past a hemisphere covered with a porous layer (case 1) or a porous ring inlay (case 2). For case 1 and case 2, the penalization parameter λ is equal to 1 (high permeability) inside the porous zone and the thickness of the porous coating is equal to $10\%d=0.1$.(a) Comparison of the 3D instantaneous (top) and 2D mean (bottom) vorticity magnitude. (b) Comparison of the drag force F_x.

that the simulations presented in this paper were realized in the domain $D=[2, 8.24] \times [-2.56, 2.56] \times [-2.56, 2.56]$. The t_{end} values reported in the table correspond to the non-dimensional final time of the simulations. Δt_{adapt}(mean) denotes the mean of the

Table 4: Parameter settings and CPU time costs for simulations of incompressible flows past a 3D hemisphere at $Re\!=\!300$ and $Re\!=\!1000$.

	Hemisphere $Re\!=\!300$	Hemisphere $Re\!=\!1000$
Resolution	512×256^2 ($\sim$ 33M pts)	1024×512^2 ($\sim$ 268M pts)
t_{end}	450	112
N time steps	42590	22352
Δt_{adapt} (mean)	$1.0\ 10^{-2}$	$5.0\ 10^{-3}$
N cores	32	64
CPU time	4 days	10 days

non-dimensional adaptative time step. This mean value is calculated on the time range $[\tilde{t}, t_{\text{end}}]$, where $\tilde{t}$ denotes the time from which the flow regime is established.

The CPU times-to-solution shown in this table correspond to a CPU time of about 40 seconds per time step on 64 cores for the high resolution $N\!=\!1024\times512^2$, and of about 8 seconds per time step on 32 cores for the lower resolution $N\!=\!512\times256^2$. This indicates a weak scalability in this range of resolutions around 80%.

Figure 14 gives the percentage of the different stages implied in the resolution of the 3D Brinkman vorticity transport equations (2.3)-(2.4), in one simulation time step for the execution on 1 core. In particular, one can notice that the FFT grid-based Poisson solver only represents 5% of the total CPU cost of one time step.
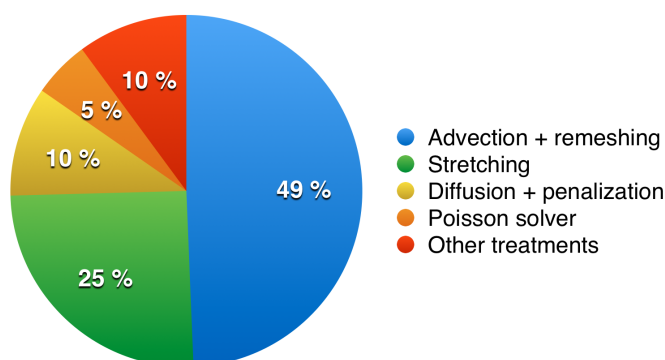

Figure 14: Percentage of the different stages implied in the resolution of the 3D penalized Vorticity-Transport-Equations (2.3)-(2.4), in one simulation time step for the execution on 1 core.

5   Conclusion

In this work, a remeshed vortex method has been employed to simulate different types of three-dimensional flows. One original feature of this vortex method relies in the remeshing process. The particle redistribution is indeed performed direction by direction, which

allows significant computational savings in 3D compared to classical tensorial approaches.

In the case of the Taylor-Green Vortex unbounded periodic flow, in which the advection and stretching phenomena are globally dominant, the low diffusivity inherent to particle methods allows to provide results close to the physics even using coarse meshes. Concerning flows past bluff bodies, we shown in this study that the present method combines the simplicity of the penalization technique and the robustness of remeshed particle methods. The penalization approach allows the modelling of solid-porous-fluid media thanks to the presence of the penalization parameter in the governing equations, without prescribing any explicit conditions at the obstacle's boundaries. This feature allowed us to apply the present method to an aerodynamic flow control problem, based on the use of porous coatings located at strategic regions on the projected surface of the body.

For both flow types, the validation studies exhibited a good agreement with references in litterature. These numerical results prove the ability of the present method to correctly account for the expected behavior of the flow at transitional or highly transitional regimes and to accurately handle immersed geometries.

A natural extension of this work concerns the derivation of a turbulence model so as to tackle simulations at higher Reynolds numbers. The challenge will then be to reach a high degree of adaptivity while keeping the simplicity and associated good scalability of the penalized remeshed particle methods.

References

[1] G.-H. Cottet and P. Koumoutsakos. *Vortex Methods-Theory and Practice*. Cambridge University Press, 2000.
[2] G.-H. Cottet. Artificial viscosity models for vortex and particle methods. *J. Comput. Phys.*, 127:199–208, 1996.
[3] O. Hald. Convergence of vortex methods II. *SIAM J. Num. Anal*, 16:726–755, 1979.
[4] J.T. Beale and A. Majda. Vortex methods II: high order accuracy in 2 and 3 dimensions. *Math. Comput.*, 32:29–52, 1982.
[5] S. Huberson and A. Jollès. Correction de l'erreur de projection dans les méthodes particules/maillage. *La recherche aérospatiale*, 4:1–6, 1990.
[6] P. Koumoutsakos and A. Leonard. High-resolution simulations of the flow around an impulsively started cylinder using vortex methods. *J. Fluid Mech.*, 296:1–38, 1995.
[7] J. P. Caltagirone. Sur l'intéraction fluide-milieu poreux : Application au calcul des efforts exercés sur un obstacle par un fluide visqueux. *C. R. Acad. Sci. Paris*, 318, 1994.
[8] P. Angot, C.-H. Bruneau and P. Fabrie. A penalization method to take into account obstacles in incompressible viscous flows. *Numer. Math.*, 81:497–520, 1999.
[9] M. Coquerelle and G.-H. Cottet. A vortex level-set method for the two-way coupling of an incompressible fluid with colliding rigid bodies. *J. Comput. Phys.*, 227:9121–9137, 2008.
[10] F. Pluvinage, A. Kourta and A. Bottaro. Instabilities in the boundary layer over a permeable, compliant wall. *Physics of Fluids*, 26, 2014.

[11] C.-H. Bruneau and I. Mortazavi. Passive control of the flow around a square cylinder using porous media. *Int. J. Numer. Meth. Fluids*, 46:415–433, 2004.

[12] C.-H. Bruneau and I. Mortazavi. Numerical modelling and passive flow control using porous media. *Comput. Fluids*, 37:488–498, 2008.

[13] N. Kevlahan and J. M. Ghidaglia. Computation of turbulent flow past an array of cylinders using a spectral method with Brinkman penalization. *Eur. J. Mech.*, B 20:333–350, 2001.

[14] D. A. Nield and A. Bejan. *Convection in Porous Media*. Springer, 1999.

[15] C. Mimeau, F. Gallizio, G.-H. Cottet and I. Mortazavi. Vortex penalization method for bluff body flows. *Int. J. Numer. Meth. Fluids*, 79:55–83, 2015.

[16] M. Gazzola, C. Mimeau, A. A. Tchieu and P. Koumoutsakos. Flow mediated interactions between two cylinders at finite re numbers. *Phys. Fluids*, 24, 043103:doi: 10.1063/1.4704195, 2012.

[17] W. M. van Rees, A. Leonard, D.I. Pullin and P. Koumoutsakos. A comparison of vortex and pseudo-spectral methods for the simulation of periodic vortical flows at high reynolds numbers. *J. Comput. Phys.*, 230(8):2794–2805, 2011.

[18] M. Gazzola, B. Hejazialhosseini and P. Koumoutsakos. Reinforcement learning and wavelet adapted vortex methods for simulations of self-propelled swimmers. *SIAM J. Sci. Comput.*, 36(3):B622–B639, 2014.

[19] G.-H. Cottet, J.-M. Etancelin, F. Perignon and C. Picard. High order semi-lagrangian particles for transport equations: numerical analysis and implementation issues. *ESAIM: Mathematical Modelling and Numerical Analysis*, 48:1029–1064, 2014.

[20] A. Magni and G.-H. Cottet. Accurate, non-oscillatory remeshing schemes for particle methods. *J. Comput. Phys.*, 231(1):152–172, 2012.

[21] P. Koumoutsakos. Multiscale flow simulations using particles. *Ann. Rev. Fluid Mechanics*, 37:457–487., 2005.

[22] C. Mimeau, G.-H. Cottet and I. Mortazavi. Direct numerical simulations of three-dimensional flows past obstacles with a vortex penalization method. *Comp & Fluids*, 136:331–347, 2016.

[23] Y. M. Kulikov and E. S. Eduard. Taylor-Green vortex simulation using CABARET scheme in a weakly compressible formulation. *Eur. Phys. J. E*, 41(3):41, 2018.

[24] S. Jammy, C. Jacobs and N. Sandham. Enstrophy and kinetic energy data from 3D Taylor-Green vortex simulations. *https://eprints.soton.ac.uk/401892/*, 2016.

[25] J. R. Bull and A. Jameson. Simulation of the Taylor-Green vortex using high-order flux reconstruction schemes. *AIAA Journal*, 53(9):2750–2761, 2015.

[26] D. Kim and H. Choi. Laminar flow past a hemisphere. *Physics of Fluids*, 15(8):2457–2460, 2003.

[27] P. Ploumhans, G. S. Winckelmans, J. K. Salmon, A. Leonard and M. S. Warren. Vortex methods for direct numerical simulation of three-dimensional bluff body flows: Applications to the sphere at *Re* = 300, 500 and 1000. *J. Comput. Phys.*, 178:427–463, 2002.

[28] F. Morency, H. Beaugendre and F. Gallizio. Aerodynamic force evaluation for ice shedding phenomenon using vortex in cell scheme, penalisation and level set approaches. *International Journal of Computational Fluid Dynamics*, 26(9–10):435–450, 2012.